# Activation of the Unfolded Protein Response and Inhibition of Translation Initiation during Coronavirus Infection

Nerea Irigoyen[1*], Krzysztof Franaszek[1], Adam M. Dinan[1,3], Nathan A. Moore[2,4], Stuart G. Siddell[2], Ian Brierley[1],Andrew E. Firth[1]

[1]Division of Virology, Department of Pathology, University of Cambridge, Tennis Court Road, Cambridge CB2 1QP, United Kingdom,

[2]Department of Cellular and Molecular Medicine, University of Bristol, Bristol BS8 1TD, United Kingdom

[3]Current address: Fios Genomics. Edinburgh BioQuarter, EH16 4UX, United Kingdom

[4]Current address: Basingstoke and North Hampshire Hospital, Hampshire Hospitals, NHS Foundation Trust

Running Title: Host translational responses to coronavirus infection

*Corresponding author: ni236@cam.ac.uk

**Keywords:** murine coronavirus, ribosome profiling, RNASeq, unfolded protein response, translation, protein synthesis

**Abstract:**

Coronaviruses (CoV), such as severe acute respiratory syndrome coronavirus (SARS-CoV) and Middle East respiratory syndrome coronavirus (MERS-CoV), are of medical importance with high mortality rates and significant zoonotic and pandemic potential. Here, we apply ribosome profiling and parallel RNASeq to globally analyse changes in the host cell translatome and transcriptome upon infection with mouse hepatitis virus, strain A59 (MHV-A59), a model murine coronavirus in the same genus as SARS-CoV and MERS-CoV. We observed translational upregulation of ATF4, ATF5 and Ddit3 and activation of the unfolded protein response (UPR). Phosphorylation of eIF2α led to the global inhibition of translation and a substantial increase in empty 80S ribosomes. A drug that inhibits the UPR attenuates virus growth suggesting that MHV may have evolved to subvert the UPR to its own advantage. We also investigated an artefact of cycloheximide pretreatment in ribosome profiling whereby ribosomes accumulate at the 5′ end of coding sequences in stressed cells but not in unstressed or untreated cells, thus extending earlier studies in yeast to mammalian cells. The study sheds light on the mechanisms of CoV translational shutoff and reveals a potential new therapeutic strategy.

**Importance:**

Ribosome profiling is an emerging technique that reveals a global snap shot of protein synthesis by precisely mapping the positions of translating ribosomes. It has particular applicability to virology where it allows not only monitoring of viral gene expression, but also host response at the level of individual genes and globally. In this work, we use ribosome profiling and parallel transcriptome sequencing (RNASeq) to monitor changes in transcription and translation in cells infected with the model coronavirus, murine coronavirus strain MHV-A59, a virus in the same genus as the medically important SARS-CoV and MERS-CoV. The sensitivity and precision of the approach permit us to obtain a high-resolution analysis of different biological processes – such as the activation of the unfolded protein response. At late time points of infection, translation is inhibited globally and, surprisingly, viral transcripts are not resistant to this effect. Nonetheless, relief of translational inhibition with a drug that interferes with the unfolded protein response is detrimental

to virus replication. This study sheds new light on the complex interactions between virus and host during infection and provides new potential targets for antiviral intervention.

## Introduction:

The *Coronaviridae* are a family of enveloped viruses with positive-sense, monopartite, single-stranded RNA genomes. At 27–32 kb, coronaviruses (CoVs) have the largest known RNA genomes. CoVs cause a broad range of diseases in animals and humans, ranging from the common cold to severe acute respiratory syndrome (SARS) [1]. Amongst CoVs of medical importance with high mortality rates and pandemic potential are SARS-CoV and MERS-CoV, both members of the genus *Betacoronavirus*. Murine coronavirus, a betacoronavirus more commonly refered to as mouse hepatitis virus (MHV), has been used as a model to study the replication and biology of other members of the genus.

Virus infection alters cellular gene expression to facilitate replication of the viral genome and the assembly of virus particles. As with all viruses, CoVs rely on the host cell translational machinery for viral protein synthesis. Many viruses have evolved mechanisms to shut-off host mRNA translation, which can increase the availability of the translational machinery for non-canonical modes of viral protein synthesis, and at the same time inhibit host antiviral responses [2]. Exactly how CoVs induce host translational shut-off and its significance in relation to the synthesis of virus proteins, particularly at later times of infection, is still poorly understood. During CoV replication, the massive production and modification of viral proteins, as well as virion budding-related endoplasmic reticulum (ER) membrane depletion, can lead to overloading of the folding capacity of the ER and, consequently, ER stress [3]. This activates the unfolded protein response (UPR) which returns the cell to homeostasis and mitigates the major risk that protein misfolding poses for correct cellular function [4]. In mammalian cells, the UPR is controlled by three ER-resident transmembrane sensors: the inositol-requiring enzyme-1 (IRE1), the PKR-like ER kinase (PERK), and the activating transcription factor-6 (ATF6). These sensors recognize unfolded/misfolded proteins inside the ER and transmit a signal to the nucleus to transcribe specific genes whose products act to lower protein synthesis and increase ER folding capacity [4]. Previous studies

(reviewed in [5]) have aimed to establish how the different UPR pathways are involved during CoV infection.Ribosome profiling (RiboSeq) allows global monitoring of cellular translation by mapping the positions of translating ribosomes on the transcriptome [6-8]. RiboSeq reveals the location and abundance of ribosomes on specific mRNA species with single-nucleotide precision. In conjunction with RNASeq, to determine the corresponding transcriptome, RiboSeq has been used to elucidate changes in translation, transcription and translation efficiency in viral and host gene expression during the course of infection [9-19].

Here, we use RiboSeq and parallel RNASeq to globally analyse changes in the host translatome and transcriptome throughout a time course of CoV infection. We observe activation of different pathways of the UPR leading to eIF2α phosphorylation and translational shut-off at the level of initiation which we confirm by polysome profiling. Surprisingly, however, a pharmacological inhibitor of the UPR was found to attenuate virus replication. We also investigate a remarkable perturbation in ribosome footprint distributions on coding sequences previously observed at late time points of infection and determine that it is a methodological artefact arising from the use of the elongation inhibitor cycloheximide. This detailed analysis of cellular translation during MHV infection provides new insights into the mechanism of CoV translational shutoff and the complex interactions between virus and host during infection, and may aid the identification of new targets for antiviral intervention.

**Results:**

**Effects of MHV-A59 infection on cellular gene expression**

To survey genome-wide changes in host translation and transcription during CoV-infection, we interrogated sequencing data generated previously in this laboratory [16]. In these experiments, we generated RNASeq and RiboSeq data from two independent biological repeats of murine 17 clone 1

cells (17 Cl-1) infected with recombinant MHV-A59 at a multiplicity of infection (MOI) of 10, and harvested at 1, 2.5, 5 and 8 h post-infection (p.i.), with mock-infected cells harvested at 1 and 8 h.

To assess the effects of MHV infection on cellular transcript abundance, differential expression analyses were performed with DESeq [20], EdgeR [21], NOISeq [22] and BaySeq ([23]). The different analyses had a large number of overlapping predictions (Fig 1A). The volcano plot (Fig 1B**)** derived from BaySeq analysis of four uninfected (1 and 8 h) and two infected (5 h p.i.) RNASeq libraries revealed that some of the most differentially expressed cellular transcripts (red points) are related to the host translational apparatus (*Eef1a1* – eukaryotic elongation factor 1A-1; *Eif3f* – eukaryotic initiation factor 3 subunit F; *Eif1* – eukaryotic initiation factor 1; *Eif2s3x* – eukaryotic initiation factor 2 subunit 3 gamma, and *Eif2b3* – eukaryotic initiation factor 2B GDP-GTP exchange factor subunit gamma), the UPR (*Herpud1* – homocysteine inducible ER protein with ubiquitin like domain 1 and *Chac1* – glutathione-specific gamma-glutamylcyclotransferase 1), and the gene coding for the largest subunit of RNA polymerase II, *Polr2a*.

To further validate changes in the transcript abundance of these genes, total RNA was extracted from three biological replicates of MHV-infected and mock-infected cells at 5 h p.i. and the levels of selected up-regulated (Fig 1C, left panel) and down-regulated (Fig 1C, middle panel) transcripts assessed by quantitative real-time PCR (qRT-PCR), normalized by a 'housekeeping gene', ribosomal protein L19 (RPL19), which has been reported to be unaffected by ER stress [24,25]. qRT-PCR was also used to assess the abundance of viral nucleocapsid (N) transcripts (Fig 1C, right panel). Up-regulated transcripts had qRT-PCR values broadly consistent with the RNASeq measurements (Fig 1B and 1C) whereas down-regulated transcripts did not, with the exception of *Eef1a*. However, the *Rpl19* transcript was, in fact, moderately down-regulated at 5 h p.i. (relative to the global transcriptome mean) (Fig 1B, yellow), which may account for these discrepancies. A comparison of differential expression between the 1 and 8 h mocks showed much smaller

differences, with only four transcripts having changes with a false discovery rate (FDR) ≤ 0.05 (S1A Fig).

CoVs induce host translational shut-off [26-31] though the mechanisms have not been well-defined. We reasoned that some host genes may be resistant to virus-induced shut-off and that identifying such genes might give new insights into the shut-off mechanism(s). To evaluate differences at the level of translation as a result of MHV infection, we calculated relative translation efficiencies (TE) – defined herein as the ratio of ribosome-protected-fragment (RPF) and total RNA density in the coding region (CDS) of a given gene – at 5 and 8 h p.i. TE was estimated using Bayseq in the paired library mode, Babel [32] and Xtail [33]. These analyses had few overlapping predictions of genes significantly differentially expressed, with Xtail producing a much higher number of predictions (Fig 2). These differences are likely due to variations in model assumptions between the different approaches and reflect the greater difficulty inherent in modeling a quotient distribution (i.e. RiboSeq/RNASeq). To proceed, we focused on genes that showed more than a 2-fold difference in mean TE between infected and mock samples, and a FDR ≤ 0.05 (upper right and upper left quadrants; Fig 2B – Babel 5 h p.i.; Fig 2C – Xtail 5 h p.i. and Xtail 8 h p.i.). Translational differences between 1 and 8 h mock-infected cells are shown in S1B Fig.

Among the mRNAs found to be preferentially translated during MHV-infection were those whose translation is known to be induced by eIF2α phosphorylation, including those for transcription factors ATF4 (activating transcription factor 4), ATF5 (activating transcription factor 5) and CHOP (DDIT3/GADD153) (Fig 2B and 2C; S2A Fig). The mRNAs encoding these proteins contain (multiple) inhibitory upstream open reading frames (uORFs) in their 5′ leaders and undergo selective re-initiation of the main ORF under conditions of eIF2α phosphorylation [34-39]. Another gene previously shown to be resistant to eIF2α phosphorylation-induced translational attenuation is Slc35a4 (Solute Carrier Family 35, Member A4; Fig 2B; [39]). In our study, the vast majority of

RPFs derived from this mRNA mapped to the 102-codon uORF (S2B Fig). These results are consistent with eIF2α phosphorylation (leading to inhibited initiation) being a major cause of host translational shut-off during MHV infection.

**An artefact of cycloheximide treatment explains a remarkable perturbation in the distribution of elongating ribosomes**

Previous meta-analyses of RPFs mapping to host mRNAs in MHV-infected cells indicated a remarkable perturbation in host cell translation at late time points [16] with a greatly increased proportion of reads mapping to the first ~30–40 codons of CDSs in MHV-infected cells at 5 and 8 h p.i. (e.g. Fig 3A compares 8 h p.i. with 8 h mock; data from [16]). Other ribosome profiling studies have revealed a similar accumulation of ribosomes in the 5′ portion of CDSs after heat shock, proteotoxic and oxidative stress, and attributed this to an early post-initiation inhibition of elongation under cell stress [40-42]. More recently, these results have been called into question by the discovery that cycloheximide pre-treatment in yeast leads to an accumulation of ribosomes in the 5′ portion of CDSs specifically in stressed cells [43,44]. Moreover, this accumulation was not seen if the yeast cells were flash frozen without cycloheximide pre-treatment, or if very high concentrations of cycloheximide were used.

In order to determine whether this experimental caveat might extend to stressed mammalian cells and perhaps explain the observed accumulation of ribosomes downstream of initiation sites during virus infection [16], 17 Cl-1 cells were infected with MHV A-59 at MOI of 10 and at 8 h p.i. harvested either by flash freezing in the absence of cycloheximide, or following supplementation of the growth medium with 100 μg/ml cycloheximide (CHX 1X) or 10 mg/ml cycloheximide (CHX 100X) for  minutes prior to harvesting. A similar experiment was performed with 17 Cl-1 cells incubated with a pharmacological inducer of ER stress, tunicamycin, for 6 h which activates all

188 UPR signalling pathways. Ribosomal occupancy profiles and the effects of stress and drug
189 treatment are shown in Fig 3B (for MHV-infected cells) and Fig 3C (for tunicamycin-treated cells).
190
191 A modest increase in ribosome occupancy downstream of initiation sites occured in tunicamycin-
192 stressed cells under normal cycloheximide treatment (compare "tunicamycin CHX 1X" with "mock
193 CHX 1X" plots; Fig 3C). Similar to findings in stressed yeast cells [43], this could be alleviated by
194 high concentrations of cycloheximide or flash freezing without cycloheximide pre-treatment (Fig
195 3C, CHX 100X and "flash frozen" plots). In virus-infected cells, however, a much more
196 pronounced accumulation of ribosomes was observed downstream of initiation sites under
197 cycloheximide treatment, and this was not alleviated even when cycloheximide was used at 100-
198 fold the normal concentration (Fig 3B**,** CHX 1X and 100X plots). However, this ribosome peak
199 completely disappeared when cells were flash frozen without cycloheximide pre-treatment (Fig 3B**,**
200 "flash frozen" plots). Thus we conclude that the cycloheximide-induced accumulation of ribosomes
201 in the 5′ region of CDSs also occurs in stressed mammalian cells and, further, that this effect is not
202 necessarily negated simply by increasing the cycloheximide concentration.
203
204 As in previous studies [41,42], we quantified excess 5′ ribosome density for individual transcripts
205 by means of a 5′ loading ratio statistic where we compared the density of RPFs in the 5′
206 approximately 30 codons of each CDS to the density of RPFs in the 3′ remainder of the CDS. As
207 expected, when harvested at 8 h in the presence of cycloheximide the 5′ loading ratios of
208 cytoplasmic mRNAs showed a substantial increase in MHV-infected cells compared to mock-
209 infected cells (Fig 4, left panel), whereas there was no such effect when cells were harvested with
210 flash freezing (Fig 4, right panel). Interestingly, but not unexpectedly, this effect was not seen for
211 mitochondrial mRNAs, which had similar 5′ loading ratio statistics over all conditions (Fig 4**,** red
212 crosses).

213 In view of the cycloheximide effect, data from the flash frozen 8 hpi mock and MHV-infected
214 samples were used for the individual gene plots shown in the following sections.
215
216 **MHV infection and activation of the unfolded protein response**
217 Although several studies [29, 45-47] have aimed to establish how each of the three UPR sensor-
218 pathways may be involved during CoV infection, we wanted to take advantage of the high-
219 resolution that ribosome profiling can provide to analyse in detail each specific arm of the UPR
220 response during MHV infection.
221
222 **Monitoring ATF6 and IRE1α activity**
223 Upon induction of ER stress, ATF6 translocates from the ER to the Golgi apparatus where it is
224 cleaved by the proteases Site-1 (S1P) and Site-2 (S2P) [48]. After cleavage, the amino-terminus of
225 ATF6, containing a basic leucine zipper (bZIP) transactivating domain, translocates to the nucleus
226 to upregulate the ER chaperone immunoglobulin heavy chain binding protein (BiP/Grp78), whose
227 mRNA or protein levels serve as a proxy for activation of the ATF6 pathway [29,49] 17 Cl-1 cells
228 were infected with MHV-A59 or incubated with tunicamycin. Cells were harvested at 2.5, 5, 8 and
229 10 h p.i. and analyzed by qRT-PCR (Fig 5A). An induction of *BiP/Grp78* transcription was
230 observed in tunicamycin-treated (purple) and MHV-infected cells (orange) from 2.5 to 8 h p.i.
231 followed by a modest decline, whereas mock-infected cells (blue) showed no induction.
232 Surprisingly, whereas Western blot analysis (Fig 5B) confirmed induction of Bip/Grp78 protein in
233 tunicamycin-treated cells by 8 h p.i., no such induction was seen in MHV-infected cells.
234
235 At 8 h p.i., MHV-infected cells were harvested by flash freezing in the absence of cycloheximide.
236 As a positive control for UPR activation, cells treated with tunicamycin for 6 h were also harvested
237 by flash freezing. RNASeq and RiboSeq read counts of *BiP/Grp78* (Mock 8 h and MHV 8 h p.i.;
238 Fig 5C) revealed an increase in RNASeq reads in MHV-infected cells (Mock RNA and Inf RNA

239 panels) consistent with the qRT-PCR results. Although an expected increase in RPFs was seen (Inf
240 Ribo panel), ribosome density was not as high in MHV-infected cells as in tunicamycin treated cells
241 (Fig 5C, Tunica Ribo panel). A lower ribosome density in the *BiP/Grp78* ORF for MHV-infected
242 cells likely explains why this protein was not immunodetected at later times of infection.
243
244 ER stress induction activates endonuclease IRE1α which cleaves X-box binding protein-1 (*Xbp-1*)
245 mRNA [50,51]. Activated IRE1α removes a 26-nt intron from unspliced *Xbp-1* (*Xbp-1u*) mRNA
246 leading to a translational reading frame shift and a longer protein. The product of spliced *Xbp-1*
247 mRNA (*XBP-1s*) is an active transcription factor that upregulates the expression of ER-associated
248 degradation (ERAD) components and ER chaperones. Determination of *Xbp-1* splicing was done by
249 reverse transcriptase PCR (RT-PCR) of total RNA extracted from 17 Cl-1 cells infected with MHV-
250 A59 or incubated with tunicamycin, using specific primers flanking the *Xbp-1* splice site (Fig 5D).
251 At all timepoints, *Xbp-1u* was the predominant form in mock-infected cells whereas *Xbp-1s* was the
252 major species in tunicamycin-treated cells. In virus-infected cells, *Xbp-1u* was predominant at 2.5 h
253 p.i. but *Xbp-1s* became predominant at 5 h p.i. In order to analyse translation of *Xbp-1u* and *Xbp-1s*
254 in virus-infected cells, we inspected the ribosome profiling data (Fig 5E). For 8 h p.i. MHV-infected
255 cells (Inf Ribo panel) and tunicamycin-treated cells (Tunica Ribo), an increased number of reads
256 mapped in the +2 reading frame (yellow peaks) of the *Xbp-1u* sequence, and downstream of the
257 annotated stop codon. These reads result from translation of the *Xbp-1s* frameshifted isoform and
258 indicate a dramatic increase in production of the active transcription factor.
259
260 **Monitoring PERK-eIF2α -ATF4 activity**
261 In response to ER stress, PERK oligomerizes and auto-phosphorylates [52]. Activated PERK
262 phosphorylates the α-subunit of eukaryotic initiation factor 2 (eIF2α) which in turn impairs
263 recycling of inactive eIF2-GDP to active eIF2-GTP resulting in a general shutdown of protein
264 synthesis [53]. However, as previously described, translation of ATF4 is increased in this situation

[34,35,54] leading to the induction of its target gene *Chop*. To monitor activation of this pathway, we analysed CHOP, ATF4 and p-eIF2α expression by qRT-PCR and Western blotting. 17 Cl-1 cells were infected with MHV-A59 or incubated with tunicamycin for 2.5, 5, 8 and 10 h. As shown in Fig 6A, *Chop* mRNA levels (measured as the *Chop/RpL19* ratio) increased five-fold in tunicamycin-treated cells (purple) compared to mock-infected cells (blue), and were stable over the time course. In MHV-infected cells (orange), the ratio also increased from 2.5 to 8 h p.i. although not to the level seen in tunicamycin-treated cells. Protein expression was determined by immunoblotting using antibodies specific for ATF4, p-eIF2α and N proteins with GAPDH and eIF2α as loading controls (Fig 6B). ATF4 and p-eIF2α were detected at all time points in tunicamycin-treated cells and all of the proteins were detected in MHV-infected cells from 5 h p.i. onwards. Subsequently, we analysed profiles of the RiboSeq and RNASeq reads mapping to ATF4 in the virus-infected and tunicamycin-treated cells (Fig 6C). Consistent with previous studies [34,35], translation of the short (three codon) uORF1 (frame +2, nucleotides 399 to 407) was observed under all conditions. In mock-infected cells, uORF2 was efficiently translated (Mock Ribo panel; reads in yellow mapping to uORF2 indicated by a yellow rectangle, frame +2) thus diverting scanning preinitiation ribosomes from accessing the main ORF (blue rectangle, frame 0, reads in purple) to which very few RPFs mapped. In contrast, in MHV-infected cells at 8 h p.i. (Inf Ribo panel), a substantial fraction of preinitation ribosomes were able to scan past uORF2 to translate the main ORF, leading to a reduced density of ribosomes on uORF2 and a greatly increased number of RPFs mapping to the main ORF. Tunicamycin-treated cells showed an intermediate ribosome distribution, but again with efficient translation of the main ORF.

Fig 6D displays the RiboSeq and RNASeq profiles for *Chop*. Consistent with the qRT-PCR analysis (Fig 6A), RNASeq reads (Inf RNA panel) were increased at 5 h p.i. compared to mock and there was an increase in the number of RPFs mapping to the main ORF (blue rectangle, purple reads). This increase in translation of the main ORF was also accompanied by an increase in the number of

RPFs derived from ribosomes initiating on the *Chop* uORF (yellow rectangle, blue reads). This uORF occupancy was especially strong in tunicamycin-treated cells (Tunica Ribo panel).

**Polysome profiling of 17 Cl-1 cells infected with MHV-A59**

Since total read counts are normalized by library size, ribosome profiling does not provide information on total global translation levels. To further investigate virus-induced inhibition of translation as a consequence of UPR activation and eIF2α phosphorylation, analytical polysome profiling (Fig 7A) was done for mock- and MHV-infected 17 Cl-1 cells. Cytoplasmic extracts were prepared in the presence of cycloheximide to retain intact monosomes and polysomes and analyzed by sucrose density gradient centrifugation. This revealed an accumulation of monosomes (80S) in MHV-infected cells from 5 h p.i. onwards, consistent with inhibition of initiation. To investigate whether the 80S ribosomes accumulating during MHV infection contain mRNA (as an indicator of a translating ribosome), polysome profiling was repeated using a higher salt buffer (400 mM KCl; Fig 7B), conditions in which 80S ribosomes lacking mRNA dissociate into constituent subunits. In mock-infected cells, a modest diminution of 80S levels was observed at 400 mM KCl (mock 5 h, compare Fig 7A panel 2, and Fig 7B left panel), but a much greater reduction in 80S was observed in MHV-infected cells (MHV 5 h p.i., compare Fig 7A panel 5 and Fig 7B right panel), indicating that the vast majority of 80S ribosomes accumulating at this time point are not mRNA-associated. These data indicate that MHV-infection leads to translational shut-off via inhibited initiation, consistent with the effects of eIF2α phosphorylation.

**Effect of the PERK inhibitor GSK-260614 on MHV replication**

GSK-260614 is a potent and selective high affinity ligand of the PERK kinase that interferes with kinase activity by competing for ATP [55,56]. In MHV-infected 17 Cl-1 cells at 5 h.p.i., the drug prevented phosphorylation of the PERK substrate, eIF2α, in a dose-dependent manner (Fig 8A**),** effectively blocking this branch of the UPR, with only a minor effect on cell viability (S4A Fig).

317 Pulse labelling of infected cells for one hour at 5 h.p.i. revealed, as expected, that prevention of
318 eIF2α phosphorylation increased modestly both viral (Fig 8A) and host protein synthesis (Fig 8B),
319 without effect on mock-infected cells (Fig 8B).
320
321 Despite the increased virus protein synthesis, 17 Cl-1 cell monolayers infected with MHV-A59 in
322 the presence of the PERK inhibitor remarkably showed delayed formation of syncytia in
323 comparison to untreated cells at 8 h p.i. (Fig 8C), and quantification of released virions through
324 $TCID_{50}$ assays revealed an ~four-fold reduction in virus titre in cells incubated with GSK-260614
325 compared to control cells (P = 0.064; S4B Fig). These observations suggest that relieving inhibition
326 of protein synthesis – affecting both cellular and viral proteins – is detrimental to virus production
327 and the development of syncytia in virus infected cells.
328
329 **Discussion:**
330
331 We have used ribosome profiling and parallel RNASeq to investigate changes in the cellular
332 translatome and transcriptome in response to infection with MHV, a representative of the
333 *Betacoronavirus* genus of the *Coronaviridae* family. These studies provide the highest resolution
334 data to date on the translatome of cells during coronavirus-induced stress.
335
336 RNASeq libraries revealed that some of the most significantly upregulated cellular transcripts in
337 virus-infected cells were part of the UPR (*Herpud1* and *Chac1*) and changes in the translation
338 efficiency of cellular proteins were consistent with uORF-regulated responses to eIF2α
339 phosphorylation, including those previously implicated as effectors of the UPR such as in *Atf4*, *Atf5*
340 and *Chop* [34-39]. These high-resolution data confirm again that there is a close interplay between
341 virus infection and the UPR, with the host activating the UPR to combat the effects of virus
342 infection, and viruses sometimes manipulating the UPR to promote replication and pathogenesis

343 [57-60]. The intimate association of CoVs with the ER during replication results in ER stress
344 responses as the cell attempts to return to homeostasis [46, 61-65; reviewed in [66]).
345
346 The relative modulation of UPR branches differs between different CoVs [3,5,66]. For example,
347 SARS-CoV infection does not lead to *Xbp-1* splicing [46] whereas the IRE1 pathway is activated by
348 infectious bronchitis virus or MHV infection or by MHV S protein overexpression [29,67]. In spite
349 of the observed *Xbp-1* mRNA splicing during MHV infection [29], Xbp-1s protein had not
350 previously been detected in coronavirus-infected cells. In our study (8 h p.i. data set), an increased
351 number of RPF reads mapped in the +2 reading frame of the *Xbp-1u* transcript corresponding to
352 translation of the *Xbp-1s* frameshifted isoform.
353
354 Activation of the ATF6 pathway by CoV infection has not yet been fully addressed. ATF6 cleavage
355 into its active form is observed during MHV infection but is significantly reduced at late time points
356 [29]. On the other hand, the trimmed ATF6 form is not detected in SARS-CoV infected cells [68].
357 Furthermore, ER stress-responsive promoters exhibit little activity under these conditions. In the
358 present study, an induction of *BiP/Grp78* transcription due to ATF6 activation was observed to a
359 similar extent in both tunicamycin-treated and MHV-infected cells, whereas BiP/Grp78 protein
360 expression was only detected by western blotting in tunicamycin-treated cells. Ribosome profiling
361 data revealed that, in virus-infected cells, the amount of RPFs corresponding to the *BiP* CDS was
362 not as high as in tunicamycin-treated cells and this was probably the reason why this protein was
363 not detected by western blot analysis.
364
365 With respect to the UPR-related inhibition mediated by eIF2α phosphorylation, it has been shown
366 that infectious bronchitis virus activates or suppresses protein kinase RNA-activated (PKR) and
367 PERK during the course of an infection [69] whereas transmissible gastroenteritis virus protein 7
368 emulates the function of DNA damage-inducible protein 34 (GADD34) to dephosphorylate eIF2α

[70]. Our study has now shown that MHV-A59 infection increases the level of p-eIF2α and ATF4 from 5 h p.i. onwards. The RiboSeq data also revealed decreased translation of the *Atf4* uORF2 at 8 h p.i. and a concomitant increase in translation of the main ORF. Although [29] failed to detect the products of ATF4 target genes, *Gadd34* and *Chop*, during MHV infection by western blotting, we found evidence supporting an increase in transcription and translation of *Chop* at later time points p.i.

We tested the effect of the selective PERK inhibitor GSK-260614 on MHV replication [55,56]. GSK-260614 ($IC_{50}$ = 0.4 nM) exhibits >1000-fold selectivity for PERK over heme-regulated eIF2α (HR1) and PKR. Up to 5 μM of this inhibitor was well tolerated by 17 Cl-1 cells and, in MHV-infected cells, the prevention of eIF2α phosphorylation alleviated the inhibition in translation of cellular and viral proteins as expected. Surprisingly, the higher content of viral proteins did not lead to a more prominent cytopathic effect but instead delayed syncytia formation and reduced viral titre. Therefore, we conclude that UPR-mediated eIF2α phosphorylation may be favourable to MHV replication – perhaps by preventing translation of various anti-viral factors – and the pharmacological manipulation of this UPR branch can be explored as a potential target for antiviral intervention.

Our previous analysis of RPFs mapping to host mRNAs during MHV infection [16] indicated a remarkable perturbation in ribosome distributions at late time points, with a greatly increased proportion of RPFs mapping to the first ~30–40 codons of coding regions. In yeast, it has been reported that an accumulation of reads in the 5′ region of coding sequences specifically under cell stress is an effect of cycloheximide pretreatment, and it has been hypothesized that stressed cells might have a slower rate of cycloheximide uptake leading to increased mean post-initiation ribosome run-on times prior to cycloheximide-induced arrest of elongation [43,44]. Thus, it was unclear whether this artefact might also occur in mammalian cells given that mammalian cells lack

a cell wall. Our results show that this does indeed extend to mammalian cells and thus call into question the interpretations put forward by [41] and [42] for the similar perturbations in ribosome density observed when cells were subjected to heat shock or proteotoxic stress. Further, we find that the magnitude of this artefact depends on the type of stress and, in the case of MHV infection, is not alleviated by increasing the concentration of cycloheximide to 100 times the standard amount, but can be alleviated completely by flash freezing without cycloheximide pretreatment. Since the artefact also occurs in mammalian cells, it is possible that it is not related simply to cycloheximide uptake rates. Potentially it may instead be related to dysregulation of the translational machinery under stress in a way that reduces cycloheximide efficiency (e.g. due to alterations in ribosomal exit (E)-site tRNA occupancy).

Ribosome profiling provides information on initiating and elongating 80S ribosomes but it does not account for free monosomes or early stages in initiation prior to formation of the 80S complex. Analytical polysome profiling showed an accumulation of 80S monosomes in MHV-infected cells from 5 h p.i. with the vast majority not being associated with mRNA which is a typical outcome of impaired translation [71]. This suggests that protein translation was inhibited at the stage of initiation probably due to the activation of the PERK branch in response to ER stress and the concomitant phosphorylation of eIF2α. Phosphorylated eIF2α (p-eIF2α) forms a stable complex with eIF2B – the guanine exchange factor responsible for recycling inactive eIF2-GDP to eIF2-GTP – which rapidly reduces the pool of available eIF2B. This prevents recycling of the ternary complex of eIF2, GTP and Met-tRNAi and formation of the 43S pre-initiation complex, and thus leads to a general shutdown of protein synthesis by inhibition of initiation [72].

Viruses commonly employ translational shutoff mechanisms to facilitate viral replication. On the one hand, shut-off of host cell translation can redirect the translation machinery towards viral gene expression if the virus has evolved non-canonical modes of translation, such as internal ribosome

entry site (IRES) mediated initiation. On the other hand, the shut-off of host cell protein synthesis will inhibit a range of cellular anti-viral responses. Previous studies have shown that MHV can induce host translational shutoff and mRNA decay in LR7 cells with the concomitant formation of stress granules and processing bodies [28]. Furthermore, a number of reports have demonstrated that CoV nsp1, the most N-terminal product of the replicase polyprotein, modulates host protein synthesis. In different CoVs, nsp1 has been shown to associate with the 40S ribosomal subunit thus preventing viral and cellular mRNA translation; induce cellular mRNA degradation via an endonucleolytic mRNA cleavage in the 5′ region of capped mRNA; and selectively target nuclear host mRNAs and transport them to the cytoplasm for degradation [30-31,73-74]. The involvement of nsp1 in host protein translation could not be ruled out in this study without a comparison with a mutant virus lacking nsp1. However, the UPR-related translational modulation and the CoV nsp1-related modification of translation (and mRNA degradation) testify to the complexity of cellular translational shutoff mechanisms utilized by CoVs. How MHV proteins can be synthesized in a state of global translation inhibition has been the subject of previous speculation. Viral mRNAs contain a common 5′-leader sequence (65–90 nucleotides long) that could bind to the nucleocapsid (N) protein to form a complex that might act as a strong translation initiation signal [75], or the leader RNA sequence may bind to nsp1, protecting the viral mRNAs from nsp1-induced RNA cleavage [74,76]. However, we found previously that virus mRNAs 2–7 were translated with generally similar efficiencies during infection and, importantly, were not preferentially translated relative to host mRNAs. Thus we concluded that the synthesis of large quantities of virus proteins, especially N, was achieved mainly through high levels of transcription [16].

In conclusion, this study provides a survey of coronavirus effects on the cellular transcriptome and translatome, complementing previous investigations on the UPR and host cell shutoff during MHV infection. The results of our analyses will help inform further investigations on host-CoV interactions and may help identify new targets for antiviral intervention.

447

448 **Materials and Methods:**

449

450 **Ribosomal profiling and RNASeq data:** Virus sequencing data (RNASeq and RiboSeq with
451 cycloheximide pretreatment) were generated previously [16] and have been deposited in the
452 ArrayExpress database (http://www.ebi.ac.uk/arrayexpress) under the accession number E-MTAB-
453 4111.
454 Data for the tunicamycin and flash freezing sequencing experiments have been deposited in
455 ArrayExpress under the accession numbers E-MTAB-5391 and E-MTAB-6278 respectively.

456

457 For the tunicamycin experiments, 17 Cl-1 cells were incubated in the presence of tunicamycin (2
458 µg/ml) and, after 6 h, cells were treated with CHX (Sigma-Aldrich; to 100 µg/ml or 10 mg/ml; 2
459 min). Cells were rinsed with 5 ml of ice-cold PBS and then submerged in a reservoir of liquid
460 nitrogen for 10 s. For flash freezing experiments, cells were rinsed with 5 ml of ice-cold PBS and
461 then submerged in liquid nitrogen for 10 s. Cell lysates were subjected to RiboSeq and RNASeq as
462 previously described [16,77].

463

464 **Computational analysis of RiboSeq and RNASeq data:** Reads were trimmed for adaptor
465 sequences, filtered for length $\geq$ 25 nt, and reads mapping to *Mus musculus* rRNA (with up to 2
466 mismatches) removed, as previously described [16]. The remaining reads were aligned directly to
467 the mouse genome (UCSC, assembly mm10) (with up to 2 mismatches) using TopHat (parameters:
468 --no-novel-juncs --bowtie1 --prefilter-multihits --max-multihits 500, with --transcriptome-index
469 defined using the genes.gtf file from the UCSC mm10 annotation available from the TopHat
470 website) [78]. Reads were tabulated using htseq-count (parameters: -t CDS -m intersection-strict -i
471 gene_id -s yes), using the NCBI RefSeq mRNAs as the gene feature annotation. For differential
472 expression analyses, the htseq-count parameter "-type CDS" was used to count only those reads

(both RiboSeq and RNASeq) that mapped to the annotated coding regions of transcripts [79]. Thus the differential expression analyses exclude reads mapping to uORFs or non-annotated coding sequences (unless such sequences overlap the main annotated ORF).

Differential expression analyses on RNASeq or RiboSeq count data were performed with DESeq [20], EdgeR [21], NOISeq [22] and BaySeq [23]. Read counts were normalized by library size prior to comparison and low count genes (genes with fewer than 1 count per million reads mapping to the CDS in either the infected or mock libraries) were discarded. For BaySeq analyses, the sample size used to calculate priors was set to 200000. For each comparison, two replicates from infected cells at a specific timepoint were compared to four libraries from uninfected cells (two each at 1 and 8 h). Changes in translation efficiency (TE) were estimated using Bayseq in the paired library mode, Babel [32] and Xtail [33]. A given gene was considered to be differentially expressed if the FDR was less than 0.05 and the fold change between the averages of infected and mock replicates was greater than two. Volcano plots and inter-replicate consistency plots were generated using standard R plotting features and FDR and log2(fold change) values from the BaySeq, Babel and Xtail analyses.

As reads were mapped to the genome, genomic read mapping locations had to be converted to transcript-specific coordinates to generate RNASeq and RPF profiles for specific transcripts. Tophat bam files were sorted by genomic coordinate and indexed using SAMTools [80]. A custom R script using Rsamtools [81] was developed to extract reads at a given series of genomic loci from the bam file (corresponding to the exon sequences of a given transcript isoform), convert the genomic positions of reads to positions relative to the transcript sequence, calculate the phasing of the reads, and generate plots showing the distribution of reads on the transcript. In some cases it is not possible to definitively distinguish usage of alternative exons or changes in transcription start sites or initiation codon utilization. The advantage of the aforementioned visualization process is that it

retains all reads mapping to a given exon allowing for easy manual inspection of data which may originate from different isoforms. In individual gene plots, read positions for RPFs were offset +12 nt to map the approximate P-site.

Histograms of 5′ end positions of host mRNA reads relative to initiation and termination codons were derived from reads mapping to RefSeq mRNAs with annotated CDSs ≥450 nt in length and with annotated 5′ and 3′ UTRs ≥60 nt in length. All figures are based on total numbers of mapped reads, rather than weighted sums for highly expressed mRNAs.

Ribosome accumulation at the 5′ end of coding sequences was assessed via a 5′ loading ratio statistic. Specifically, the density of RPFs with estimated P-sites mapping within nucleotide positions 16–90 of a given ORF was compared with the density of reads in the downstream portion of the ORF (ending 15 nt before the ORF stop codon). These windows were designed to exclude the accumulation of ribosomes involved in initiation and termination. We then compared the loading ratio in infected samples with the loading ratio in mocks for each gene.

**Cells and virus:** Murine 17 clone 1 (17 Cl-1) ([82], a kind gift of Dr Stanley Sawicki, University of Toledo) cells were maintained in Dulbecco's modification of Eagle's medium supplemented with 10% (vol/vol) fetal calf serum (FCS). Recombinant MHV strain A59 (MHV-A59) was derived as previously described ([83], a kind gift of Dr Stanley Sawicki, University of Toledo, ATCC VR764). Upon reaching 70–80% confluence, 17 Cl-1 cells were infected with MHV-A59 at MOI 10 in infection medium [Hank's balanced salt solution (HBSS) containing 50 µg/ml DEAE-dextran and 0.2% bovine serum albumin (BSA)]. After 45 min at 37 ºC, the inoculum was removed and the cells were incubated in DMEM containing 10% FCS, 100 U/ml penicillin and 100 µg/ml streptomycin at 37 ºC until harvest.

524 17 Cl-1 mock and MHV-infected cells were treated with different concentrations (1–5 μM) of the
525 PERK-inhibitor GSK-2606414, a kind gift of Dr Edward Emmott and Prof Ian Goodfellow. GSK-
526 2606414 was added to the cells just after the adsorption time and maintained until cells were
527 harvested.
528
529 **Quantitative real-time PCR assays:** Total RNA was isolated as described previously [76] for
530 RNA-Seq analysis, and cDNA was synthesized from 1 μg total RNA. Transcript levels were
531 determined by quantitative real-time PCR using a Rotor-Gene 3000 (Corbett Research). Reactions
532 were performed in a final volume of 20 μl containing Hot Start Taq (1 U; QIAGEN), 3.5 mM
533 $MgCl_2$, 2.5 mM deoxynucleotides, SYBR Green dye, 500 nM forward and reverse specific primers
534 and 1 μl of cDNA. After enzyme activation (95 °C, 15 min), amplification was carried out in a
535 three-step PCR procedure (50 cycles: 15 s at 95 °C for denaturation, 20 s at 55 ºC for annealing and
536 20 s at 72 °C for extension). Non-template controls were included for each primer pair, and each
537 PCR reaction was carried out in triplicate.
538
539 **Immunoblotting:** Proteins were separated by 10% or 12% SDS-PAGE and transferred to
540 nitrocellulose membranes. These were blocked (5% non-fat milk powder in PBST [137 mM NaCl,
541 2.7 mM KCl, 10 mM $Na_2HPO_4$, 1.5 mM $KH_2PO_4$, pH 6.7, and 0.1% Tween 20]) and probed with
542 mouse monoclonal antibodies raised against N (1:1,000), S (1:500) - kind gifts of Dr Helmut Wege,
543 University of Würzburg -, GAPDH (G8795, Sigma-Aldrich, 1:20,000), S6 (1:500, Cell Signaling);
544 rabbit monoclonal antibodies against Grp78/BiP (1:1,000, Abcam) and RPL10a (1:500, Abcam); or
545 polyclonal rabbit anti-ATF4 (1:500, Proteintech), anti-eIF2α and anti-p(Ser-51)-eIF2α (1:1,000,
546 Cell Signaling). Membranes were incubated in the dark with an IRDye-conjugated secondary
547 antibody in phosphate-buffered saline (PBS) and 0.1% Tween 20 [IRDye 800CW Donkey Anti-
548 Mouse IgG (H+L), IRDye 800CW Donkey Anti-Rabbit IgG (H+L), IRDye 680RD Goat Anti-

549 Mouse IgG (H+L) and IRDye 680RD Goat Anti-Mouse IgM (μ chain specific)]. Blots were
550 scanned using an Odyssey Infrared Imaging System (Licor).
551
552 **Polysome profiling:** 17 Cl-1 cells were infected as previously described. Ten minutes prior to
553 harvesting, cells were treated with cycloheximide (100 μg/ml), washed with PBS and lysed in a
554 buffer containing 20 mM Tris HCl pH 7.5, 100 mM KCl, 5 mM MgOAc, 0.375 mM CHX, 1 mM
555 DTT, 0.1 mM PMSF, 2U/μl DNase I, 0.5% NP-40, supplemented with protease and phosphatase
556 inhibitors (ThermoFisher Scientific). Following trituration with a 26-G needle (ten passes), lysates
557 were cleared (13,000 *g* at 4 ºC for 20 min) and the supernatants layered onto 12 mL sucrose density
558 gradients (10–50% sucrose in TMK buffer – 20 mM Tris-HCl pH 7.5, 100 mM KCl, 5 mM $MgCl_2$)
559 prepared in Beckman SW41 polypropylene tubes using a Gradient Master (Biocomp). Following
560 centrifugation (200,000 *g* for 90 min at 4 ºC), fractions were prepared using an ISCO fractionator
561 monitoring absorbance at 254 nm. Proteins were concentrated from fractions using methanol-
562 chloroform extraction [84] and subjected to immunoblotting analysis. Polysome profiling in higher
563 salt conditions was carried out as described above except that the lysis buffer and sucrose density
564 gradient contained 400 mM KCl.
565
566 **Metabolic labelling:** 17 Cl-1 cell monolayers were infected with MHV A-59 at a MOI of 10
567 PFU/cell. At 5 h p.i., cells were washed twice with PBS and labelled for 1 h in methionine-free
568 DMEM supplemented with 125 μCi/ml [$^{35}$S] methionine. After this period, cells were harvested,
569 washed twice with PBS and resuspended in lysis buffer (50 mM Tris pH 7.5, 100 mM NaCl, 5 mM
570 EDTA, 0.5% NP40). Cell lysate aliquots were mixed with Laemmli's sample buffer to a final
571 concentration of 1× and subjected to 10% SDS-PAGE followed by autoradiography.
572
573 **References:**

574 1. Channappanavar R, Perlman S (2017) Pathogenic human coronavirus infections: causes and
575 consequences of cytokine storm and immunopathology. Semin Immunopathol. doi:
576 10.1007/s00281-017-0629-x.

2. Walsh D, Mathews MB, Mohr I (2013) Tinkering with translation: protein synthesis in virus-infected cells. Cold Spring Harb Perspect Biol 5:a012351.

3. Fung TS, Liu DX (2014) Coronavirus infection, ER stress, apoptosis and innate immunity. Front Microbiol 5: 296.

4. Ron D, Walter P (2007) Signal integration in the endoplasmic reticulum unfolded protein response. Nat Rev Mol Cell Biol 8: 519-529.

5. Fung TS, Liao Y, Liu DX (2016) Regulation of stress responses and translational control by coronavirus. Viruses 8: E184.

6. Ingolia NT, Ghaemmaghami S, Newman JR, Weissman JS (2009) Genome-wide analysis in vivo of translation with nucleotide resolution using ribosome profiling. Science 324: 218-223.

7. Ingolia NT, Lareau LF, Weissman JS (2011) Ribosome profiling of mouse embryonic stem cells reveals the complexity and dynamics of mammalian proteomes. Cell 147: 789-802.

8. Ingolia NT (2014) Ribosome profiling: new views of translation, from single codons to genome scale. Nat Rev Genet 15: 205-213.

9. Stern-Ginossar N, Weisburd B, Michalski A, Le VT, Hein MY, Huang SX, Ma M, Shen B, Qian SB, Hengel H, et al (2012) Decoding human cytomegalovirus. Science 338: 1088-1093.

10. Liu X, Jiang H, Gu Z, Roberts, JW (2013) High-resolution view of bacteriophage lambda gene expression by ribosome profiling. Proc Natl Acad Sci U S A 110: 11928-11933.

11. Arias C, Weisburd B, Stern-Ginossar N, Mercier A, Madrid AS, Bellare P, Holdorf M, Weissman JS, Ganem D (2014) KSHV 2.0: a comprehensive annotation of the Kaposi's sarcoma-associated herpesvirus genome using next-generation sequencing reveals novel genomic and functional features. PLoS Pathog 10: e1003847.

12. Rutkowski AJ, Erhard F, L'Hernault A, Bonfert T, Schilhabel M, Crump C, Rosenstiel P, Efstathiou S, Zimmer R, Friedel CC, et al (2015) Widespread disruption of host transcription termination in HSV-1 infection. Nat Commun 6: 7126.

13. Tirosh O, Cohen Y, Shitrit A, Shani O, Le-Trilling VT, Trilling M, Friedlander G, Tanenbaum M, Stern-Ginossar N (2015) The transcription and translation landscapes during human cytomegalovirus infection reveal novel host-pathogen interactions. PLoS Pathog 11: e1005288.

14. Yang Z, Cao S, Martens CA, Porcella SF, Xie Z, Ma M, Shen B, Moss B (2015) Deciphering poxvirus gene expression by RNA sequencing and ribosome profiling. J Virol 89: 6874-6886.

15. Bercovich-Kinori A, Tai J, Gelbart IA, Shitrit A, Ben-Moshe S, Drori Y, Itzkovitz S, Mandelboim M, Stern-Ginossar N (2016) A systematic view on influenza induced host shutoff. Elife 5: e18311.

16. Irigoyen N, Firth AE, Jones JD, Chung BY, Siddell SG, Brierley I (2016) High-resolution analysis of coronavirus gene expression by RNA sequencing and ribosome profiling. PLoS Pathog 12: e1005473.

17. Dai A, Cao S, Dhungel P, Luan Y, Liu Y, Xie Z, Yang Z (2017) Ribosome profiling reveals translational upregulation of cellular oxidative phosphorylation mRNAs during vaccinia virus-induced host shutoff. J Virol 91: e01858.16.

18. Irigoyen N, Dinan AM, Brierley I, Firth AE (2018) Ribosome profiling of the retrovirus murine leukemia virus. Retrovirology 15: 10.

19. Reid DW, Campos RK, Child JR, Zheng T, Chan KWK, Bradrick SS, Vasudevan SG, Garcia-Blanco MA, Nicchitta CV (2018) Dengue virus selectively annexes endoplasmic reticulum-associated translation machinery as a strategy for co-opting host cell protein synthesis. J Virol 92:e01766-17.

20. Anders S, Reyes A, Huber W (2012) Detecting differential usage of exons from RNA-seq data. Genome Res 22: 2008-2017.

21. Robinson MD, McCarthy DJ, Smyth GK (2010) edgeR: a Bioconductor package for differential expression analysis of digital gene expression data. Bioinformatics 26: 130-140.

22. Tarazona S, Furió-Tarí P, Turrà D, Pietro AD, Nueda MJ, Ferrer A, Conesa A (2015) Data quality aware analysis of differential expression in RNA-seq with NOISeq R/Bioc package. Nucleic Acids Res 43: e140.

23. Hardcastle TJ, Kelly KA (2010) baySeq: empirical Bayesian methods for identifying differential expression in sequence count data. BMC Bioinformatics 11: 422.

24. Hollien J, Weissman JS (2006) Decay of endoplasmic reticulum-localized mRNAs during the unfolded protein response. Science 313: 104-107.

25. Hiramatsu N, Joseph VT, Lin JH (2011) Monitoring and manipulating mammalian unfolded protein response. Methods Enzymol 491: 183-198.

26. Siddell SG, Wege H, Barthel, A, ter Meulen V (1980) Coronavirus JHM: cell-free synthesis of structural protein p60. J Virol 33: 10-17.

27. Hilton A, Mizzen L, MacIntyre G, Cheley S, Anderson R (1986) Translational control in murine hepatitis virus infection. J Gen Virol 67: 923-932.

28. Raaben M, Groot Koerkamp MJ, Rottier PJ, de Haan CA (2007) Mouse hepatitis coronavirus replication induces host translational shutoff and mRNA decay, with concomitant formation of stress granules and processing bodies. Cell Microbiol 9: 2218-2229.

29. Bechill J, Chen Z, Brewer JW, Baker SC (2008) Coronavirus infection modulates the unfolded protein response and mediates sustained translational repression. J Virol 82: 4492-4501.

30. Kamitani W, Huang C, Narayanan K, Lokugamage KG, Makino S (2009) A two-pronged strategy to suppress host protein synthesis by SARS coronavirus Nsp1. Nat Struct Mol Biol 16: 1134-1140.

31. Lokugamage KG, Narayanan K, Nakagawa K, Terasaki K, Ramirez SI, Tseng CT, Makino S (2015) Middle east respiratory syndrome coronavirus nsp1 inhibits host gene expression by selectively targeting mRNAs transcribed in the nucleus while sparing mRNAs of cytoplasmic origin. J Virol 89: 10970-10981.

32. Olshen AB, Hsieh AC, Stumpf CR, Olshen RA, Ruggero D, Taylor BS (2013) Assessing gene-level translational control from ribosome profiling. Bioinformatics 29: 2995-3002.

33. Xiao Z, Zou Q, Liu Y, Yang X (2016) Genome-wide assessment of differential translations with ribosome profiling data. Nat Commun 7: 11194.

34. Lu PD, Harding HP, Ron D (2004) Translation reinitiation at alternative open reading frames regulates gene expression in an integrated stress response. J Cell Biol 167: 27-33.

35. Vattem KM, Wek RC (2004) Reinitiation involving upstream ORFs regulates ATF4 mRNA translation in mammalian cells. Proc Natl Acad Sci U S A 101: 11269-11274.

36. Watatani Y, Ichikawa K, Nakanishi N, Fujimoto M, Takeda H, Kimura N, Hirose H, Takahashi S, Takahashi Y (2008) Stress-induced translation of ATF5 mRNA is regulated by the 5′-untranslated region. J Biol Chem 283: 2543-2553.

37. Zhou D, Palam LR, Jiang L, Narasimhan J, Staschke KA, Wek RC (2008) Phosphorylation of eIF2 directs ATF5 translational control in response to diverse stress conditions. J Biol Chem 283: 7064-7073.

38. Palam LR, Baird TD, Wek RC (2011) Phosphorylation of eIF2 facilitates ribosomal bypass of an inhibitory upstream ORF to enhance CHOP translation. J Biol Chem 286: 10939-10949.

39. Andreev DE, O'Connor PB, Fahey C, Kenny EM, Terenin IM, Dmitriev SE, Cormican P, Morris DW, Shatsky IN, Baranov PV (2015) Translation of 5′leaders is pervasive in genes resistant to eIF2 repression. Elife 4: e03971.

40. Gerashchenko MV, Lobanov AV, Gladyshev VN (2012) Genome-wide ribosome profiling reveals complex translational regulation in response to oxidative stress. Proc Natl Acad Sci U S A 109: 17394-17399.

41. Liu B, Han Y, Qian SB (2013) Cotranslational response to proteotoxic stress by elongation pausing of ribosomes. Mol Cell 49: 453-463.

42. Shalgi R, Hurt JA, Krykbaeva I, Taipale M, Lindquist S, Burge CB (2013) Widespread regulation of translation by elongation pausing in heat shock. Mol Cell 49: 439-452.

43. Gerashchenko MV, Gladyshev VN (2014) Translation inhibitors cause abnormalities in ribosome profiling experiments. Nucleic Acids Res 42: e134.

44. Duncan CDS, Mata J (2017) Effects of cycloheximide on the interpretation of ribosome profiling experiments in Schizosaccharomyces pombe. Sci Rep 7: 10331.

45. Jiang XS, Tang LY, Dai J, Zhou H, Li SJ, Xia QC, Wu JR, Zeng R (2005) Quantitative analysis of severe acute respiratory syndrome (SARS)-associated coronavirus-infected cells using proteomic approaches: implications for cellular responses to virus infection. Mol Cell Proteomics 4: 902-913.

46. Versteeg GA, van de Nes PS, Bredenbeek PJ, Spaan WJ (2007) The coronavirus spike protein induces endoplasmic reticulum stress and upregulation of intracellular chemokine mRNA concentrations. J Virol 81: 10981-10990.

47. Yeung YS, Yip CW, Hon CC, Chow KY, Ma IC, Zeng F, Leung FC (2008) Transcriptional profiling of Vero E6 cells over-expressing SARS-CoV s2 subunit: insights on viral regulation of apoptosis and proliferation. Virology 371: 32-43.

48. Ye J, Rawson RB, Komuro R, Chen X, Davé UP, Prywes R, Brown MS, Goldstein JL (2000) ER stress induces cleavage of membrane-bound ATF6 by the sames proteases that process SREBPs. Mol Cell 6: 1355-1364.

49. Haze K, Yoshida H, Yanagi H, Yura U, Mori K (1999) Mammalian transcription factor ATF6 is synthesized as a transmembrane protein and activated by proteolysis in response to endoplasmic reticulum stress. Mol Biol Cell 10:3787-3799.

50. Yoshida H, Matsui T, Yamamoto A, Okada T, Mori K (2001) XBP1 mRNA is induced by ATF6 and spliced by IRE1 in response to ER stress to produce a highly active transcription factor. Cell 28: 881-891.

51. Calfon M, Zeng H, Urano F, Till JH, Hubbard SR, Harding HP, Clark SG, Ron D (2002) IRE1 couples endoplasmic reticulum load to secretory capacity by processing the XBP-1 mRNA. Nature 415: 92-96.

52. Harding HP, Zhang Y, Ron D (1999) Protein translation and folding are coupled by an endoplasmic-reticulum-resident kinase. Nature 397: 271-274.

53. Harding HP, Zhang Y, Bertolotti A, Zeng H, Ron D (2000) Perk is essential for translational regulation and cell survival during the unfolded protein response. Mol Cell 5: 897-904.

54. Harding HP, Novoa I, Zhang Y, Zeng H, Wek R, Schapira M, Ron D (2000) Regulated translation initiation controls stress-induced gene expression in mammalian cells. Mol Cell 6: 1099-1108.

55. Axten JM, Medina JR, Feng Y, Shu A, Romeril SP, Grant SW, Li WH, Heerding DA, Minthorn E, Mencken T, Atkins C, Liu Q, Rabindran S, Kumar R, Hong X, Goetz A, Stanley T, Taylor JD, Sigethy SD, Tomberlin GH, Hassell AM, Kahler KM, Shewchuk LM, Gampe RT (2012) Discovery of 7-methyl-5-(1-{[3-(trifluoromethyl)phenyl]acetyl}-2,3-dihydro-1H-indol-5-yl)-7H-pyrrolo[2,3-d]pyrimidin-4-amine (GSK2606414), a potent and selective first-in-class inhibitor of protein kinase R (PKR)-like endoplasmic reticulum kinase (PERK). J Med Chem *55*, 7193-7207.

56. Harding HP, Zyryanova AF, Ron D (2012) Uncoupling proteostasis and development in vitro with a small molecule inhibitor of the pancreatic endoplasmic reticulum kinase, PERK. J Biol Chem *287*, 44338-44344.

57. Lazar C, Uta M, Branza-Nichita N (2014) Modulation of the unfolded protein response by the human hepatitis B virus. Front Microbiol 5: 433.

58. Carpenter JE, Grose C (2014) Varicella-zoster glycoprotein expression differentially induces the unfolded protein response in infected cells. Front Microbiol 5: 322.

59. Chan SW (2014) The unfolded protein response in virus infections. Front Microbiol 5: 518.

60. Perera N, Miller JL, Zitzmann N (2017) The role of the unfolded protein response in dengue virus pathogenesis. Cell Microbiol 19: doi: 10.1111/cmi.12734

61. David-Ferreira JF, Manaker RA (1965) An electron microscopy study of the development of a mouse hepatitis virus in tissue culture cells. J Cell Biol 24: 57-78.

62. Klumperman J, Locker JK, Meijer A, Horzinek MC, Geuze HJ, Rottier PJ (1994) Coronavirus M proteins accumulate in the Golgi complex beyond the site of virion budding. J Virol 68: 6523-6534.

63. Stertz S, Reichelt M, Spiegel M, Kuri T, Martínez-Sobrido L, García-Sastre A, Weber F, Kochs G (2007) The intracellular sites of early replication and budding of SARS-coronavirus. Virology 361: 304-315.

64. Reggiori F, Monastyrska I, Verheije MH, Calì T, Ulasli M, Bianchi S, Bernasconi R, de Haan CA, Molinari M (2010) Coronaviruses hijack the LC3-I-positive EDEMosomes, ER-derived vesicles exporting short-lived ERAD regulators, for replication. Cell Host Microbe 7: 500-508.

65. Maier HJ, Hawes PC, Cottam EM, Mantell J, Verkade P, Monaghan P, Wileman T, Britton P (2013) Infectious bronchitis virus generates spherules from zippered endoplasmic reticulum membranes. MBio 4: e00801-13.

66. Fung TS, Liao Y, Liu DX (2014) The endoplasmic reticulum stress sensor IREa protects cells from apoptosis induced by the coronavirus infectious bronchitis virus. J Virol 88: 12752-12764.

67. Fung TS, Huang M, Liu DX (2014) Coronavirus-induced ER stress response and its involvement in regulation of coronavirus-host interactions. Virus Res 194: 110-123.

68. DeDiego ML, Nieto-Torres JL, Jiménez-Guardeño JM, Regla-Nava JA, Alvarez E, Oliveros JC, Zhao J, Fett C, Perlman S, Enjuanes L (2011) Severe acute respiratory syndrome coronavirus envelope protein regulates cell stress response and apoptosis. PLoS Pathog 7: e1002315.

69. Liao Y, Fung TS, Huang M, Fang SG, Zhong Y, Liu DX (2013) Upregulation of CHOP/GADD153 during coronavirus infectious bronchitis virus infection modulates apoptosis by restricting activation of the extracellular signal-regulated kinase pathway. J Virol 87: 8124-8134.

70. Cruz JL, Sola I, Becares M, Alberca B, Plana J, Enjuanes L, Zuñiga S (2011) Coronavirus gene 7 counteracts host defenses and modulates virus virulence. PLoS Pathog 7: e1002090.

71. Brina D, Grosso S, Miluzio A, Biffo S (2011) Translational control by 80S formation and 60S availability: the central role of eIF6, a rate limiting factor in cell cycle progression and tumorigenesis. Cell Cycle *10*, 3441-3446.

72. Hinnebusch AG (2014) The scanning mechanism of eukaryotic translation initiation. Annu Rev Biochem *83*, 779-812.

73. Kamitani W, Narayanan K, Huang C, Lokugamage K, Ikegami T, Ito N, Kubo H, Makino S (2006) Severe acute respiratory syndrome coronavirus nsp1 protein suppresses host gene expression by promoting host mRNA degradation. Proc Natl Acad Sci U S A 103: 12885-12890.

74. Huang C, Lokugamage KG, Rozovics JM, Narayanan K, Semler BL, Makino S (2011) SARS coronavirus nsp1 protein induces template-dependent endonucleolytic cleavage of mRNAs: viral mRNAs are resistant to nsp1-induced RNA cleavage. PLoS Pathog 7: e1002433.

75. Tahara SM, Dietlin TA, Bergmann CC, Nelson GW, Kyuwa S, Anthony RP, Stohlman SA (1994) Coronavirus translational regulation: leader affects mRNA efficiency. Virology 202: 621-630.

76. Tanaka T, Kamitani W, DeDiego ML, Enjuanes L, Matsuura Y (2012) Severe acute respiratory syndrome coronavirus nsp1 facilitates efficient propagation in cells through a specific translational shutoff of host mRNA. J Virol 86: 11128-11137.

77. Chung BY, Hardcastle TJ, Jones JD, Irigoyen N, Firth AE, Baulcombe DC, Brierley I (2015) The use of duplex-specific nuclease in ribosome profiling and a user-friendly software package for Ribo-seq data analysis. RNA 21: 1731-1745.

78. Trapnell C, Pachter L, Salzberg SL (2009) TopHat: discovering splice junctions with RNA-Seq. Bioinformatics 25: 1105-1111.

79. Anders S, Pyl PT, Huber W (2015) HTSeq - a Python framework to work with high-throughput sequencing data. Bioinformatics 31: 166-169.

80. Li H, Handsaker B, Wysoker A, Fennell T, Ruan J, Homer N, Marth G, Abecasis G, Durbin R; 1000 Genome Project Data Processing Subgroup (2009) The sequence alignment/map format and SAMtools. Bioinformatics 25: 2078-2079.

81. Delhomme N, Padioleau I, Furlong EE, Steinmetz LM (2012) easyRNASeq: a bioconductor package for processing RNA-Seq data. Bioinformatics 28: 2532-2533.

82. Sturman LS, Takemoto KK (1972) Enhanced growth of a murine coronavirus in transformed mouse cells. Infect Immun 6: 501-507.

83. Coley SE, Lavi E, Sawicki SG, Fu L, Schelle B, Karl, N, Siddell SG, Thiel V (2005) Recombinant mouse hepatitis virus strain A59 from cloned, full-length cDNA replicates to high titers in vitro and is fully pathogenic *in vivo*. J Virol 79: 3097-3106.

84. Eckert EA (1966) Envelope protein(s) derived from influenza virus. J Bacteriol 91: 1907-1910.

**Figure Captions:**

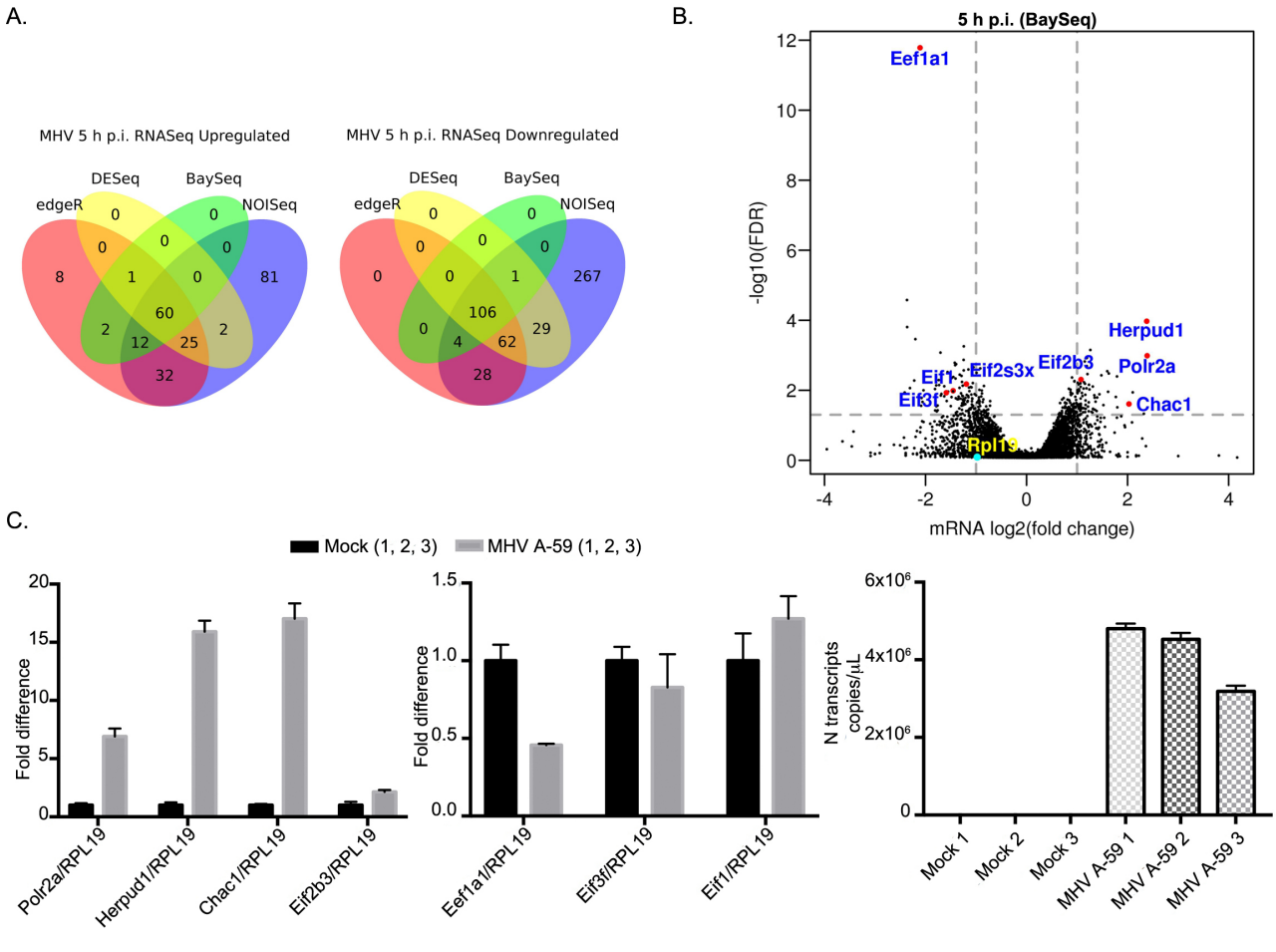


**Figure 1: Effect of MHV infection on cellular transcription. (A)** Venn diagrams of upregulated (left panel) and downregulated (right panel) genes were derived from RNASeq data using four different methods (edgeR, DESeq, BaySeq and NOISeq). A gene was considered to be up/downregulated if it had ≥2 fold change and a FDR ≤ 0.05. Calculations are based on four mock (two each at 1 and 8 h) and two 5 h p.i. infected samples. **(B)** Volcano plot showing the relative change in abundance of cellular genes and the FDR for differential expression using BaySeq. Grey vertical and horizontal lines indicate a fold change of 2 and a FDR of 0.05, respectively. Selected genes are annotated. (**C**) Quantitative real-time PCR (qRT-PCR) of N transcripts (right panel), and selected down- (middle panel), and up- (left panel) regulated mRNAs in three biological replicates of mock- and MHV-infected cells at 5 h p.i. Levels were normalized to ribosomal protein L19 (RPL19) transcript.

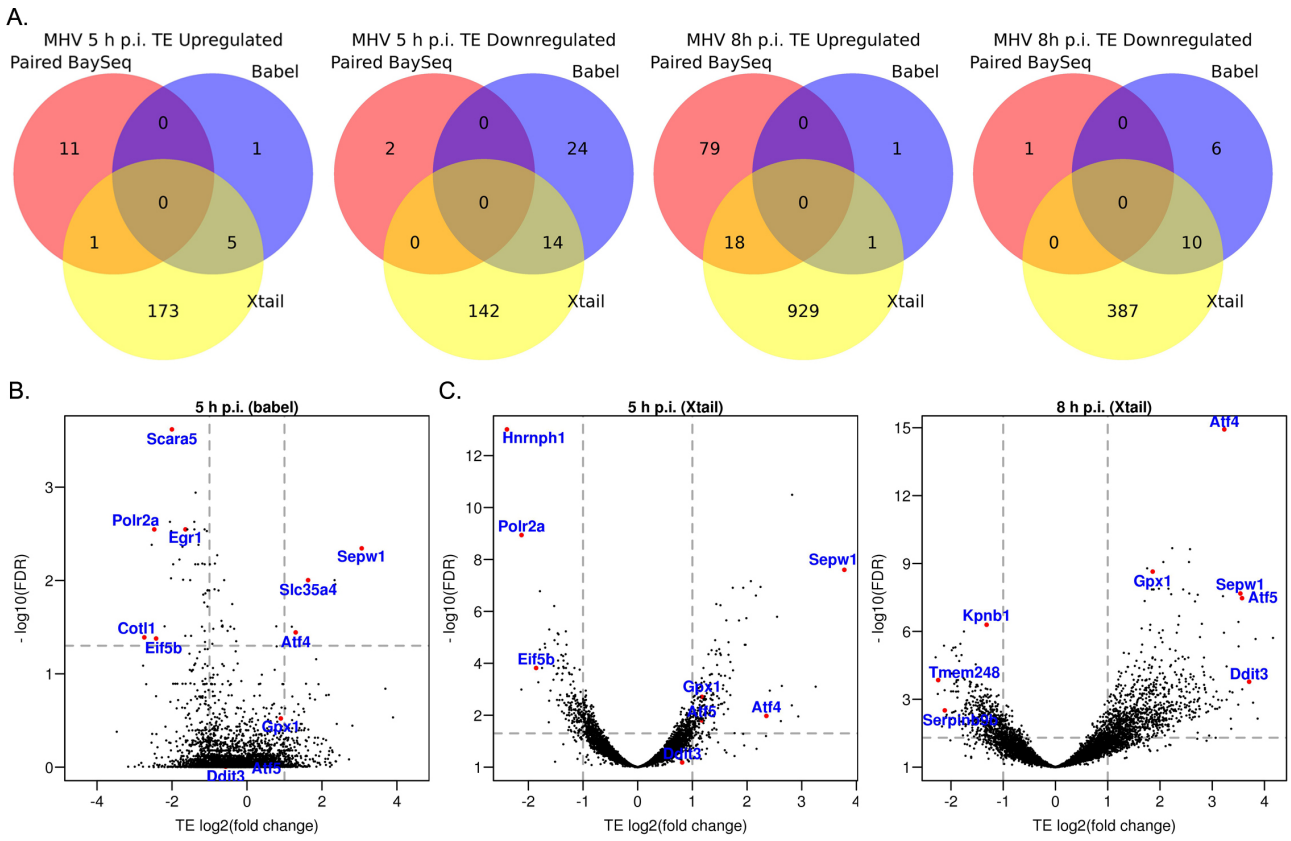


884

885 **Figure 2: Effects of MHV infection on translational efficiency (TE). (A)** Venn diagrams of TE
886 upregulated and downregulated genes using three different methods (Babel, Xtail and paired
887 BaySeq) at 5 h p.i. (left panels) and 8 h p.i. (right panels). A gene was considered to be
888 up/downregulated if it had ≥2 fold change and a FDR ≤ 0.05. Calculations are based on four
889 RiboSeq/RNASeq pairs of mock (two each at 1 and 8 h) and two RiboSeq/RNASeq pairs of 5 or 8 h
890 p.i. infected samples. **(B-C)** Volcano plots showing the relative change in TE for cellular genes and
891 the FDR for differential expression using Babel or Xtail.

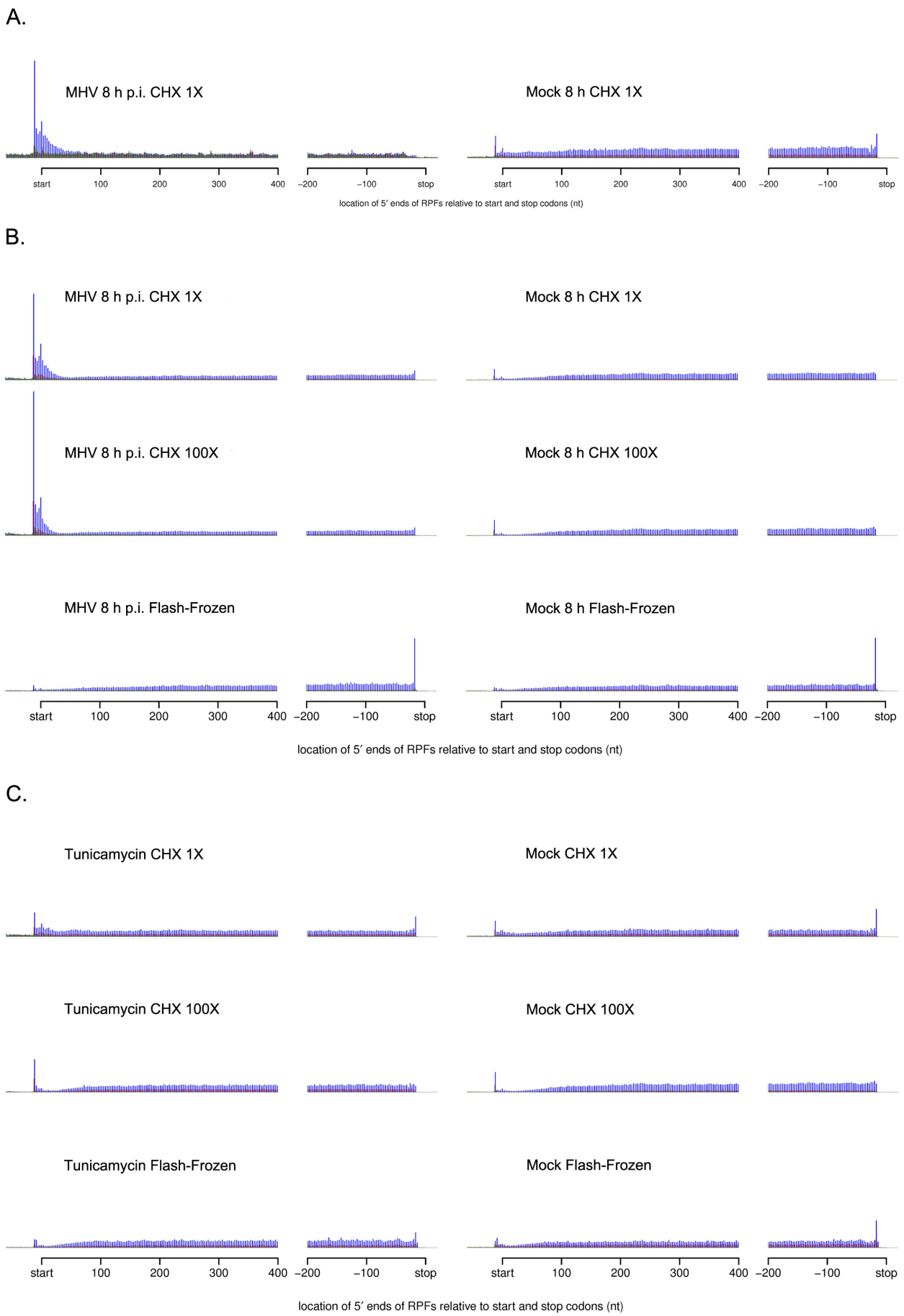


**Figure 3: Effects of cycloheximide on ribosome profiling of 17 Cl-1 cells infected with MHV-A59. (A)** Mean RPF density on cellular mRNAs (arbitrary *y*-axis scaling). In the MHV 8 h p.i.

895 RiboSeq library, an increased proportion of reads map to the first ~30–40 codons of CDSs (data
896 from [16]). **(B)** Meta-analysis of RPFs mapping to cellular mRNAs of 17 Cl-1 cells (right panels)
897 and 8 h p.i. MHV-infected 17 Cl-1 cells (left panels), harvested with 100 µg/ml cycloheximide
898 (CHX 1X) or 10 mg/ml cycloheximide (CHX 100X) in the media or harvested by flash freezing in
899 the absence of cycloheximide. **(C)** Meta-analysis of RPFs mapping to cellular mRNAs of 17 Cl-1
900 cells (right panels) and 17 Cl-1 cells treated with tunicamycin (2 µg/ml final concentration for 6 h)
901 (left panels), harvested with 100 µg/ml cycloheximide (CHX 1X) or 10 mg/ml cycloheximide
902 (CHX 100X) in the media or harvested by flash freezing in the absence of cycloheximide.
903

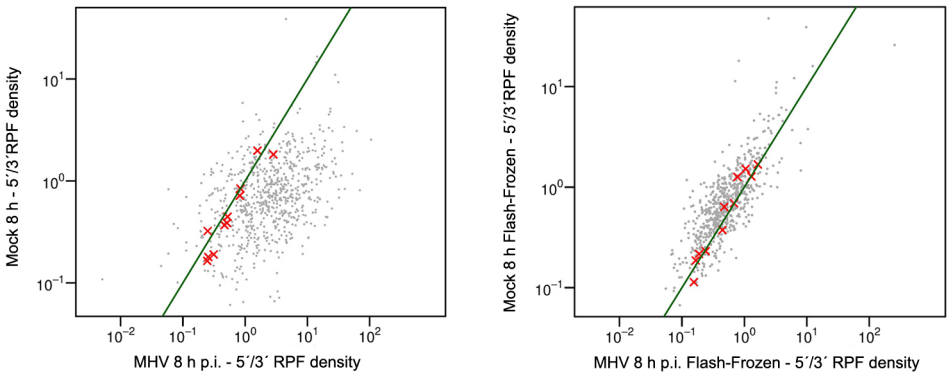


904

905 **Figure 4: Quantification of ribosome accumulation via a 5′ loading ratio statistic.** Scatterplot
906 comparing the relative density of RPFs in the 5′ and 3′ portions of cellular mRNA CDSs between
907 mock and 8 h p.i. infected samples harvested with 100 µg/ml cycloheximide (left panel) or by flash
908 freezing (right panel). Only genes with ≥50 RPFs mapping between CDS positions 16 and 90 nt in
909 the 8 h mock are shown. Points below the green diagonal line indicate mRNA species with
910 increased ribosome density in the 5′regions of coding sequences in infected cells compared to
911 mock. Red crosses represent mitochondrial CDSs.

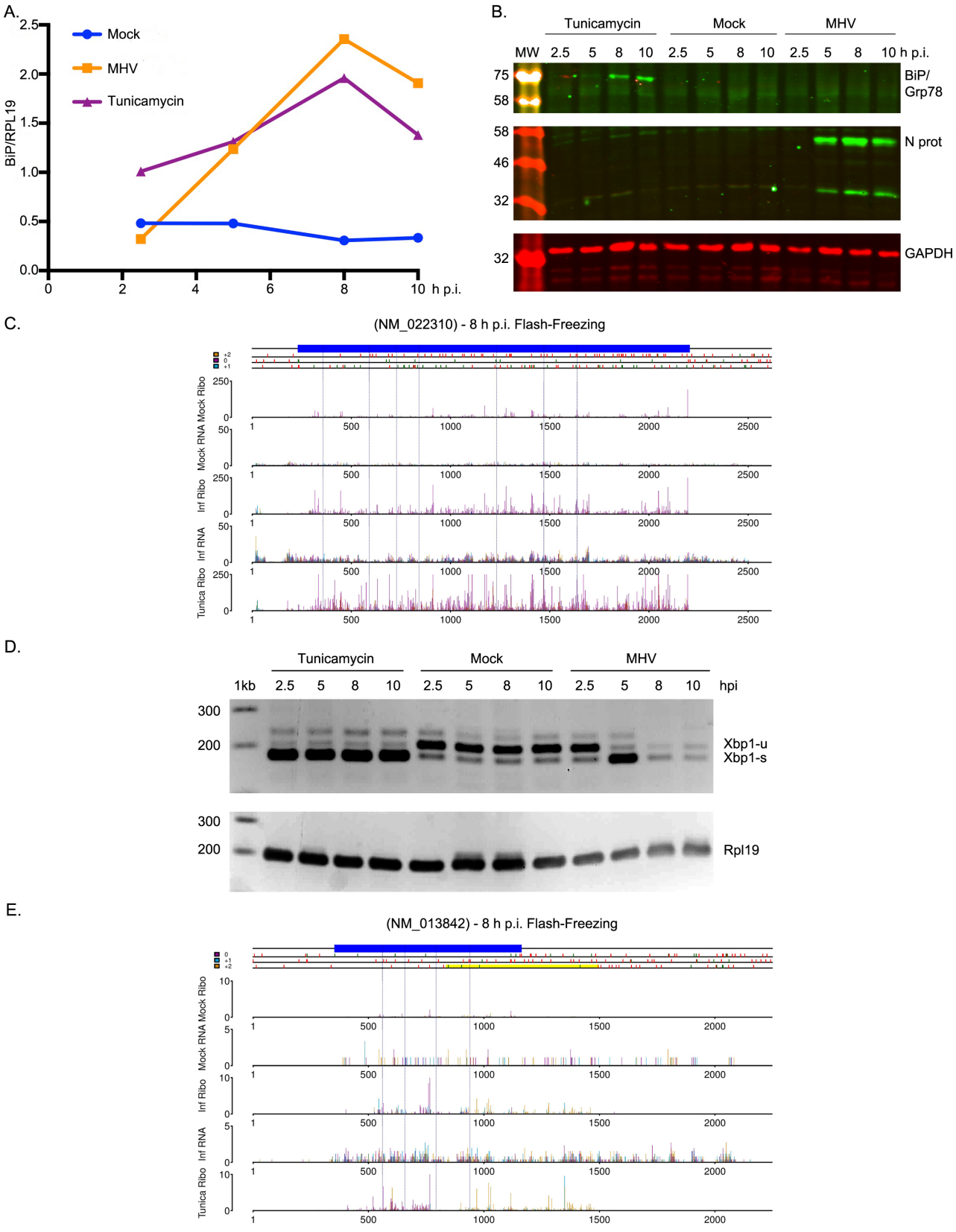


**Figure 5: Effect of MHV infection on unfolded protein response ATF6 and IRE 1α activity.** 17 Cl-1 cells were incubated in the presence of tunicamycin (2 µg/ml) or infected with MHV-A59 (MOI 10) and harvested at 2.5, 5, 8 and 10 h p.i. (**A**) qRT-PCR of *BiP*/*Grp78* transcripts normalized

916 by *Rpl19* transcript. (**B**) Cell lysates were analysed by 12% SDS-PAGE and immunoblotted using
917 anti-BiP/Grp78 and anti-N antibodies (green fluorescent secondary antibody). GAPDH was used as
918 a loading control (red fluorescent secondary antibody). Molecular masses (kDa) are indicated on the
919 left. (**C**) Analysis of RPFs (Mock Ribo, Inf Ribo and Tunica Ribo) and RNASeq (Mock RNA and
920 Inf RNA) mapping to *BiP/Grp78*, also known as *Hspa5* (NCBI RefSeq mRNA NM_022310)
921 showing, from top to bottom, mock 8 h (Mock), MHV 8 h p.i. (Inf) and tunicamycin treated
922 (Tunica) cells harvested by flash-freezing. Reads whose 5′ end maps to the first, second or third
923 positions of codons relative to the annotated CDS (blue rectangle) are indicated in purple, blue or
924 orange, respectively. Green and red tick marks correspond to AUG and stop codons, respectively.
925 Blue dotted vertical lines indicate annotated exon boundaries. The *y*-axis shows reads per million
926 mapped to host mRNAs. Note that in order to properly visualize RPFs across the *BiP/Grp78* ORF,
927 the *y*-axis has been truncated leaving some RPF counts for tunicamycin-treated cells off scale. S3
928 Fig shows the non-modified gene-plot for *BiP/Grp78*. (**D**) RT-PCR analysis of *Xbp-1u* and *Xbp-1s*
929 mRNAs. Total RNA (1μg) was subjected to RT-PCR analysis using primers flanking the *Xbp-1*
930 splice site. PCR products were resolved in a 3% TBE-agarose gel and visualized by ethidium
931 bromide staining. *Rpl19* RT-PCR product was used as a loading control. Molecular size markers
932 (nt) are indicated on the left. Note as gel loads are normalised by total RNA concentration, Xbp-1
933 mRNA levels appear to diminish at late timepoints in samples from MHV infected cells, as the
934 increased viral RNA levels decrease the relative proportion of Xbp1 transcripts in the load. (**E**)
935 Analysis of RPFs (Mock Ribo, Inf Ribo and Tunica Ribo) and RNASeq (Mock RNA and Inf RNA)
936 mapping to *Xbp-1u* (NCBI RefSeq mRNA NM_013842) showing, from top to bottom, mock 8 h
937 (Mock), MHV 8 h p.i. (Inf) and tunicamycin treated (Tunica) cells harvested by flash-freezing.
938 Reads whose 5′ end maps to the first, second or third positions of codons relative to the annotated
939 *Xbp-1u* CDS (blue rectangle) are indicated in purple, blue or orange, respectively. Yellow
940 rectangles indicate the extended ORF in *Xbp-1s*. Green and red tick marks, and blue dotted vertical

941 lines are as described in Fig 5C. Note that reads in the +2 frame downstream of the annotated stop
942 codon (yellow peaks) are derived from translation of the *Xbp-1s* spliced isoform.

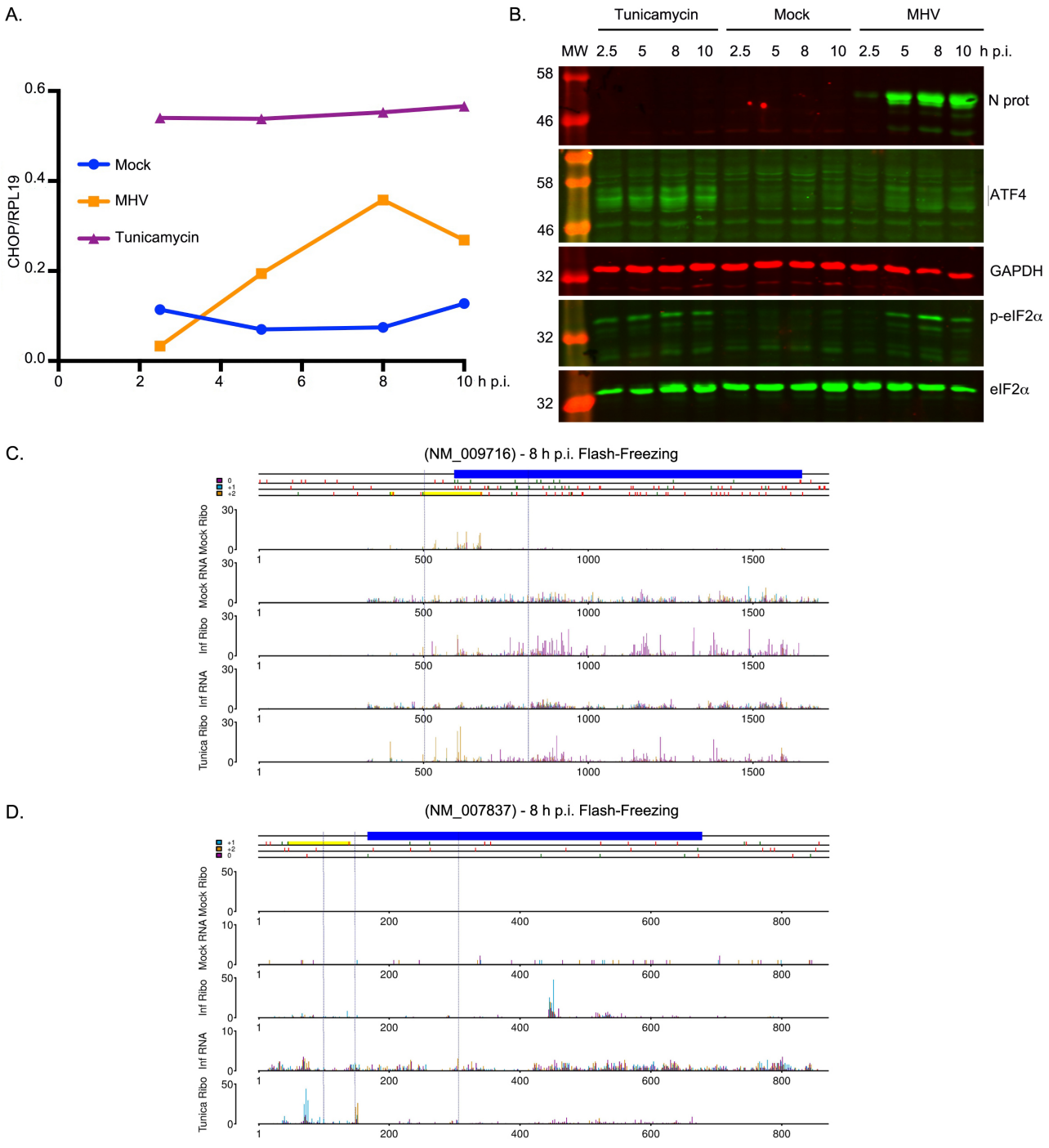


943

944 **Figure 6: Effect of MHV infection on unfolded protein response PERK-eIF2α-ATF4 activity.**
945 17 Cl-1 cells were incubated in the presence of tunicamycin (2 µg/ml) or infected with MHV-A59
946 (MOI 10) and harvested at 2.5, 5, 8 and 10 h p.i. (**A**) qRT-PCR of *Chop* transcripts normalized by
947 *Rpl19* transcript. (**B**) Cell lysates were separated by 12% SDS-PAGE and immunoblotted using

anti-ATF4, anti-p-eIF2α, anti-eIF2α and anti-N antibodies (green fluorescent secondary antibody). GAPDH was used as a loading control (red fluorescent secondary antibody). Molecular masses (kDa) are indicated on the left. (**C**) Analysis of RPFs (Mock Ribo, Inf Ribo and Tunica Ribo) and RNASeq (Mock RNA and Inf RNA) mapping to *Atf4* (NCBI RefSeq mRNA NM_009716) showing, from top to bottom, mock 8 h (Mock), MHV 8 h p.i. (Inf) and tunicamycin treated (Tunica) cells harvested by flash freezing. Reads whose 5′ end maps to the first, second or third positions of codons relative to the annotated CDS (blue rectangle) are indicated in purple, blue or orange, respectively. Yellow rectangles indicate the *Atf4* uORFs. Green and red tick marks, and blue dotted vertical lines are as described in Fig 5C. (**D**) Analysis of RPFs (Mock Ribo, Inf Ribo and Tunica Ribo) and RNASeq (Mock RNA and Inf RNA) mapping to *Chop*, also known as *Ddit3* (NCBI RefSeq mRNA NM_007837) showing, from top to bottom, mock 8 h (Mock), MHV 8 h p.i. (Inf) and tunicamycin treated (Tunica) cells harvested by flash freezing. Reads whose 5′ end maps to the first, second or third positions of codons relative to annotated CDS (blue rectangle) are indicated in purple, blue or orange, respectively. Green and red tick marks, and blue dotted vertical lines are as described in Fig 5C. Note that reads in the +1 frame upstream of the annotated start codon (blue reads) are derived from translation of the *Chop* uORF (yellow rectangle).

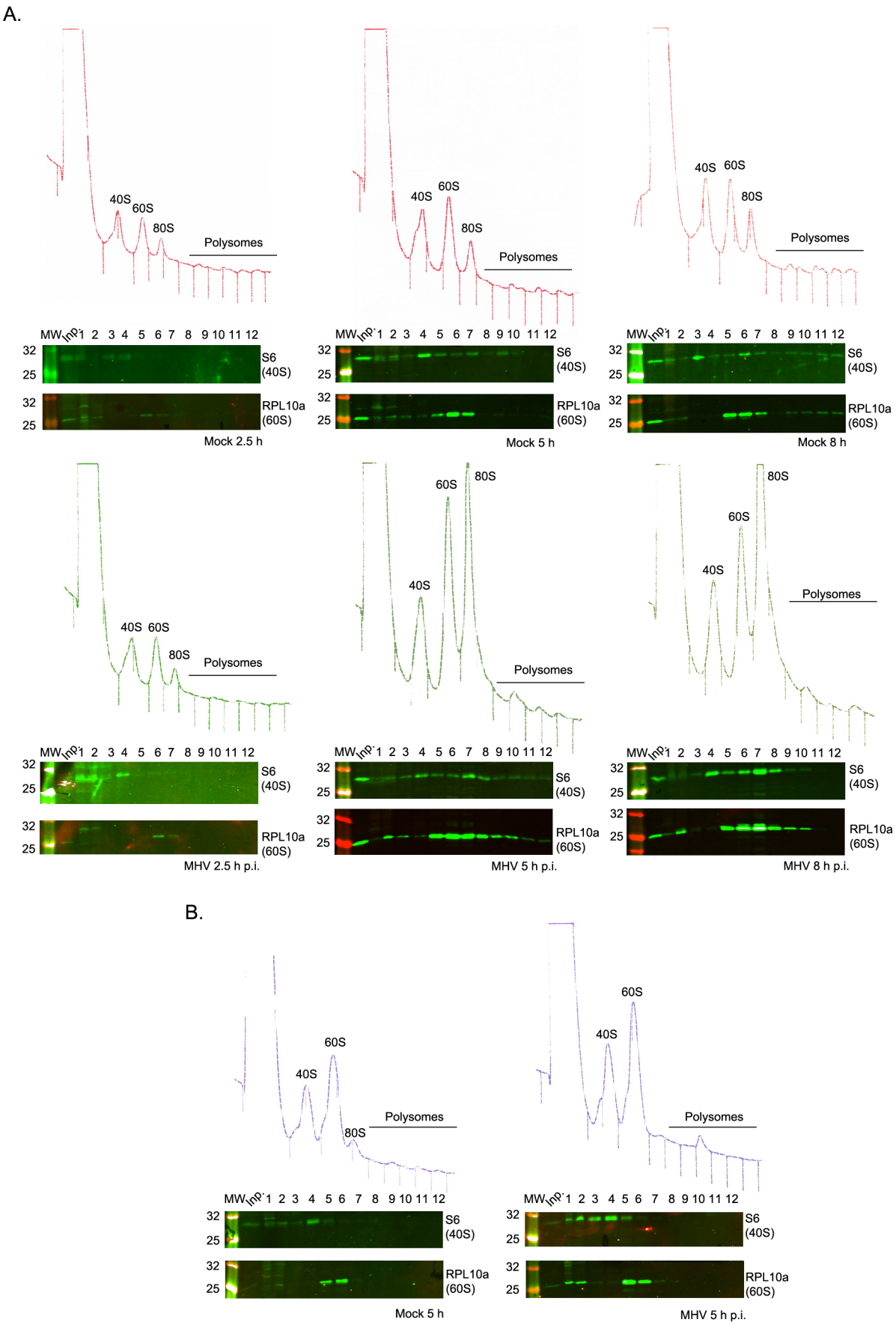


964
965 **Figure 7: Polysome profiling of 17 Cl-1 cells infected with MHV-A59.** (**A**) Mock-infected (upper
966 panel) and MHV-infected (lower panel) 17 Cl-1 cells were harvested at 2.5, 5 and 8 h p.i.

967 Cytoplasmic lysates were resolved on 10–50% sucrose density gradients. Gradients were
968 fractionated and fractions monitored by absorbance ($A_{254}$ nm). Twelve [numbered] fractions were
969 collected and proteins extracted, resolved by 12% SDS-PAGE and analysed by immunoblotting
970 using the indicated antibodies (anti-S6 as 40S marker, anti-RPL10 as 60S marker, anti-N and anti-
971 S). (**B**) Mock-infected (left panel) and MHV-infected (right panel) 17 Cl-1 cells were harvested at 5
972 h p.i. in high-salt lysis buffer (400 mM KCl) and analysed as described above. Molecular masses
973 (kDa) are indicated on the left. Lane "Inp" contains whole cell lysate.

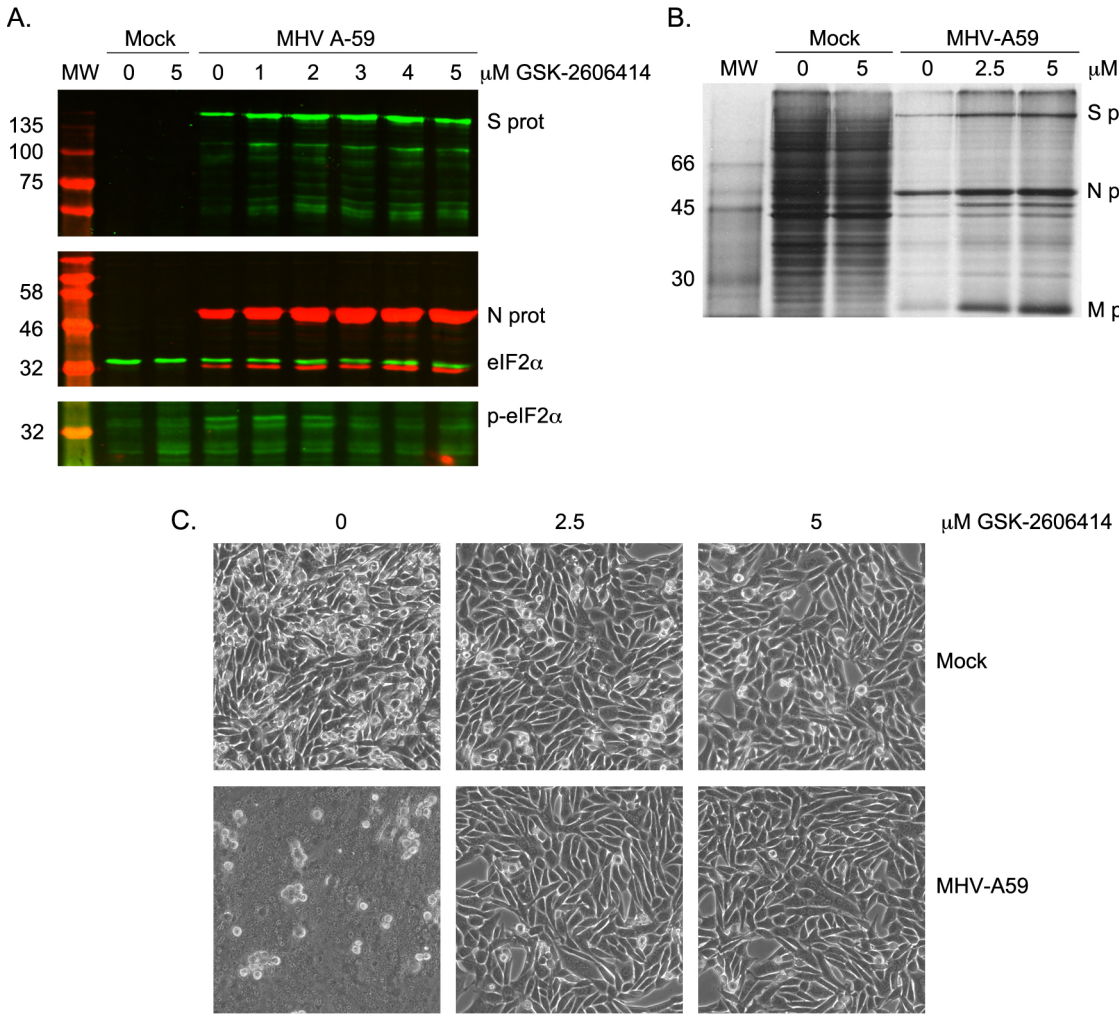


974

975 **Figure 8: Effect of GSK-2606414 on MHV-infected cells.** (**A**) 17 Cl-1 mock and MHV-infected
976 cells were treated with 1–5 μM of the PERK-inhibitor GSK-2606414. GSK-2606414 was added to
977 the cells immediately after the virus adsorption period was completed and maintained in the
978 medium until cells were harvested 5 h later. Cell lysates were separated by 12% SDS-PAGE and

immunoblotted using anti-S, anti-p-eIF2α and anti-eIF2α (green fluorescent secondary antibody), and anti-N sera (red fluorescent secondary antibody). Molecular masses (kDa) are indicated on the left. (**B**) 17 Cl-1 cells infected with MHV-A59 and treated with 0, 2.5 or 5 μM of GSK-2606414 were metabolically pulse-labeled with [$^{35}$S]Met for 1 h at 5 h p.i. Cells were lysed just after pulse and subjected to 10% SDS-PAGE followed by autoradiography. (**C**) Representative images of mock and MHV-infected cells at 5 h p.i. treated with 0, 2.5 or 5 μM of GSK-2606414.